Iterative Methods for Solving the Nonlinear Balance Equation with Optimal Truncation

Qin XU[1*] and Jie CAO[2,3]

[1]*NOAA/National Severe Storms Laboratory, Norman, Oklahoma, USA*

[2]*Cooperative Institute for Mesoscale Meteorological Studies, University of Oklahoma, Norman, Oklahoma, USA*

[3]*Institute of Atmospheric Physics, Chinese Academy of Sciences, Beijing* 100029

(Submitted to *Adv. Atmos. Sci.*, 8/26/2020, revised 11/15/2020, accepted 12/20/2020)

----

* Corresponding author: Qin Xu
E-mail: Qin.Xu@noaa.gov

ABSTRACT

Two types of previous iterative methods for solving the nonlinear balance equation (NBE) are revisited. In the first type, the NBE is rearranged into a linearized equation for a presumably small correction to the initial guess or the subsequent updated solution. In the second type, the NBE is rearranged into a quadratic form of the absolute vorticity with the positive root of this quadratic form used in the form of Poisson equation to solve NBE iteratively. The two methods are re-derived by expanding the solution asymptotically upon a small Rossby number, and a criterion for optimally truncating the asymptotic expansion is proposed to obtain the super-asymptotic approximation of the solution. For each re-derived method, two iterative procedures are designed using the integral-form Poisson solver versus the over-relaxation scheme to solve the boundary value problem in each iteration. Tested with analytically formulated wavering jet flows on the synoptic, sub-synoptic and meso-α scales, the iterative procedure designed for the first method with the Poisson solver, named M1a, is found to be the most accurate and efficient. For the synoptic wavering jet flow in which the NBE is entirely elliptic, M1a is extremely accurate. For the sub-synoptic wavering jet flow in which the NBE is mostly elliptic, M1a is sufficiently accurate. For the meso-α wavering jet flow in which the NBE is partially hyperbolic so its boundary value problem becomes seriously ill-posed, M1a can effectively reduce the solution error for the cyclonically curved part of the wavering jet flow but not for the anti-cyclonically curved part.

Keywords: nonlinear balance, iterative method, optimal truncation

Article Highlights:

- Two previous iterative methods for solving the NBE are re-derived by expanding the solution asymptotically upon a small Rossby number *Ro*.
- A criterion for optimal truncation of asymptotic expansion is proposed to obtain the super-asymptotic approximation of the solution.
- Using the integral-form Poisson solver for the boundary value problem in each iteration, optimally truncated solutions can be obtained efficiently with improved accuracies.
- Solution errors can be reduced effectively even when *Ro* increases to 0.4 for cyclonically curved jet flows of meso-α scale.

1. Introduction

For flows of synoptic and sub-synoptic scales in the middle and high latitudes, the nonlinear balance equation (NBE) links the streamfunction field with the geopotential field more accurately than the geostrophic balance (Charney, 1955; Bolin, 1955). However, solving the streamfunction from the NBE for a given geopotential field can be very challenging due to complicated issues on the existence of solution in conjunction with difficulties caused by nonlinearity (Courant and Hilbert, 1962). It is well known mathematically that the NBE is a special case of the Monge-Ampere differential equation for the streamfunction (Charney, 1955). If the geostrophic vorticity (that is, the vorticiy of geostrophic flow associated with the given geopotential field) is larger than $-f/2$ for a constant f where f is the Coriolis parameter, then the NBE is of the elliptic type and its associated boundary value problem can have no more than two solutions (see Section 6.3 in Chapter 4 of Courant and Hilbert, 1962). If the geostrophic vorticity is smaller than $-f/2$ in a local area, then the NBE becomes locally hyperbolic. In this case, the boundary value problem becomes ill-posed and thus may have no solution although the NBE can be integrated along the characteristic lines within the locally hyperbolic area (see Section 3 of Appendix I in Chapter 5 of Courant and Hilbert, 1962).

To avoid the complication and difficulties caused by the local non-ellipticity in solving the NBE, one can simply enforce the ellipticity condition to a certain extent by slightly smoothing or adjusting the given geopotential field. This type of treatment has been commonly used in previously developed iterative methods to solve the NBE as a boundary value problem (Bolin, 1955, 1956; Shuman, 1955, 1957; Miyakoda, 1956; Bushby and Huckle, 1956; Arnason, 1958;

Bring and Charasch, 1958; Liao and Chow, 1962; Asselin, 1967; Paegle and Tomlinson, 1975; Bijlsma and Hoogendoorn, 1983). However, regardless of the above treatment, the convergence properties of the previous iterative methods or any iterative methods can be not only scale-dependent but also flow-dependent and thus very difficult to study theoretically and rigorously.

The above reviewed previous iterative methods can be classified into two types. In the first type (originally proposed by Bolin, 1955), the NBE is transformed into a linearized equation for a presumably small correction to the initial guess or to the subsequent updated solution when this linearized equation is solved iteratively. In the second type (originally proposed by Shuman, 1955, 1957; Miyakoda, 1956), the NBE is rearranged into a quadratic form of the absolute vorticity and the positive root of this quadratic form is used in the form of Poisson equation to solve for the streamfunction iteratively. The initial guess for both types is the geostrophic streamfunction. Their convergence properties were analyzed theoretically, but the analysis was lack of rigor and generality, because the coefficients of linearized differential operator for the first type and the forcing terms on the right-hand side of the iterative form of linearized equation for the second type were functions of space but treated as constants (Arnason, 1958; Bijlsma and Hoogendoorn, 1983). Therefore the convergence properties of the previously iterative methods were examined mainly through numerical experiments. Besides, due to the very limited computer memories and speed in those early decades, the previous iterative methods employed the memory-saving sequential relaxation scheme based on the classical Liebmann-type iteration algorithm (Southwell, 1946) and applied to coarse resolution grids for large-scale flows. The sequential relaxation and successive over-relaxation (SOR) schemes have been used in the second type of iterative method (Shuman, 1955, 1957) to solve the NBE for hurricane flows (Zhu et al., 2002). However, using the previous iterative methods to solve the NBE still faces various difficulties especially when the spatial scale reduces to and even below the sub-synoptic scale. In particular, there are unaddressed challenging issues concerning whether and how the solutions can be obtained approximately and efficiently through limited numbers of iterations, especially when the NBE becomes locally hyperbolic (due mainly to reduced spatial scales) and thus the iterative methods fail to converge.

This paper aims to address the above concerned challenging issues. In particular, we will re-derive the above two types of iterative methods formally and systematically by expanding the solution asymptotically upon a small Rossby number and substituting it into the NBE. Since the asymptotic expansion is not ensured to converge especially when the Rossby number is not sufficiently small, the concept of optimal truncation of asymptotic expansion is employed and a criterion is proposed for optimal truncation to obtain the super-asymptotic approximation of the solution based on the heuristic theory of asymptotic analysis (Boyd, 1999). As will be seen in this paper, by employing the optimal truncation, the issue on non-convergence of the iterative methods caused by the increase of Rossby number can be addressed to a certain extent. Besides, the recently developed Poisson solver based on integral formulas (Xu et al., 2011; Cao and Xu, 2011) will be used in comparison with the aforementioned classical SOR scheme to solve the boundary value problem in each iterative step. In particular, for flows of sub-synoptic scale or meso-α scale, the NBE can become locally hyperbolic and the solution will be checked in this paper via the proposed optimal truncation under certain conditions.

The paper is organized as follows. The next section presents formal and systematical derivations of the above reviewed two iterative methods. Section 2 formulates the criterion for optimal truncation, and section 3 constructs four different iterative procedures with optimal truncation and designs numerical experiments for testing the iterative procedures. Section 4 examines and compares the results of experiments performed with the four iterative procedures, followed by conclusions in section 5.

2. Derivations of two iterative methods

2.1 Scaling and asymptotic expansion based on small Rossby number

The NBE can be written into the following form (Charney, 1955):

$$N(\psi) = \nabla^2\phi, \tag{1a}$$

where $N(\psi) \equiv \nabla^2\psi + (\nabla\psi)\cdot\nabla f + 2J_{xy}(\partial_x\psi, \partial_y\psi) = \nabla\cdot(f\nabla\psi) + 2J_{xy}(\partial_x\psi, \partial_y\psi) = \nabla^2(f\psi) - \nabla\cdot(\psi\nabla f) + 2J_{xy}(\partial_x\psi, \partial_y\psi)$, ψ is the streamfunction, ϕ is the geopotential, $\nabla \equiv (\partial_x, \partial_y)$, $\nabla^2 \equiv \nabla\cdot\nabla = \partial_x^2 + \partial_y^2$, and $J_{xy}(\partial_x\psi, \partial_y\psi) \equiv (\partial_x^2\psi)(\partial_y^2\psi) - (\partial_x\partial_y\psi)^2$. For large-scale and synoptic-scale flows, the geostrophic approximation, $\nabla^2\phi \approx \nabla^2(f\psi)$, is the leading-order balance in (1a) and thus $\nabla^2(f\psi)$ is the dominant term in $N(\psi)$. In this case, the boundary condition for solving ψ from (1a) over a middle-latitude domain D can be given by

$$\psi = \psi_g \quad \text{on } \partial D, \tag{1b}$$

where ∂D denotes the domain boundary, and $\psi_g \equiv \phi/f$ is the global geostrophic streamfunction

(Kuo, 1959; Charney and Stern, 1962; Schubert et al., 2009).

Formally, we can scale x and y by L, scale $f = f_o + f'$ by f_o, and scale ψ and ϕ by UL and f_oUL, respectively, where U is the horizontal velocity scale, L is the horizontal length scale, f_o is a constant reference value of f which can be the value of f at the domain center. The scaled variables are still denoted by their respectively original symbols, so the NBE can have the following non-dimensional form:

$$\nabla^2(f\psi - \phi) = \nabla\cdot(\psi\nabla f') - R_o 2J_{xy}(\partial_x\psi, \partial_y\psi), \tag{2}$$

where $R_o \equiv U/f_oL$ is the Rossby number. For synoptic-scale and sub-synoptic-scale flows, the above scaling can give $R_o = \varepsilon < 1$. Substituting this into (2) gives

$$\nabla^2(f\psi - \phi) = \varepsilon[\nabla\cdot(\psi\nabla F) - 2J_{xy}(\partial_x\psi, \partial_y\psi)], \tag{3}$$

where $F = f'/(f_oR_o) \leq O(1)$ and O( ) is the 'order-of-magnitude' symbol. Thus, ψ can have the following asymptotic expansion:

$$\psi = \psi_0 + \sum\nolimits_{\underline{1}} \varepsilon^k \delta\psi_k, \tag{4}$$

where $\psi_0 = \psi_g$ and $\sum_{\underline{1}}$ denotes the summation over k from 1 to ∞. The k^{th} order truncation of the asymptotic expansion of ψ in (4) is given by $\psi_k \equiv \psi_0 + \sum_{\underline{1}}^k \varepsilon^{k'} \delta\psi_{k'}$, where $\sum_{\underline{1}}^k$ denotes the summation over k' from 1 to k. Formally, $\psi = \psi_k + O(\varepsilon^{k+1})$, so ψ_k is accurate up to $O(\varepsilon^k)$ as an approximation of ψ.

By substituting (4) into (3) and (1b), and then collecting terms of the same order of ε, we obtain

$$\nabla^2(f\delta\psi_1) = \nabla\cdot(\psi_0\nabla F) - 2J_{xy}(\partial_x\psi_0, \partial_y\psi_0),$$

$$\nabla^2(f\delta\psi_2) = \nabla\cdot(\delta\psi_1\nabla F) - 2[J_{xy}(\partial_x\psi_0, \partial_y\delta\psi_1) + J_{xy}(\partial_x\delta\psi_1, \partial_y\psi_0)],$$

$$\nabla^2(f\delta\psi_3) = \nabla\cdot(\delta\psi_2\nabla F) - 2[J_{xy}(\partial_x\psi_0, \partial_y\delta\psi_2) + J_{xy}(\partial_x\delta\psi_2, \partial_y\psi_0) + J_{xy}(\partial_x\delta\psi_1, \partial_y\delta\psi_1)],$$

$$\nabla^2(f\delta\psi_4) = \nabla\cdot(\delta\psi_3\nabla F) - 2[J_{xy}(\partial_x\psi_0, \partial_y\delta\psi_3) + J_{xy}(\partial_x\delta\psi_3, \partial_y\psi_0)$$

$$+ J_{xy}(\partial_x\delta\psi_1, \partial_y\delta\psi_2) + J_{xy}(\partial_x\delta\psi_2, \partial_y\delta\psi_1)],$$

$$\ldots$$

$$\nabla^2(f\delta\psi_{k+1}) = \nabla\cdot(\delta\psi_k\nabla F) - 2[J_{xy}(\partial_x\psi_0, \partial_y\delta\psi_k) + J_{xy}(\partial_x\delta\delta\psi_k, \partial_y\psi_0) + J_{xy}(\partial_x\delta\psi_1, \partial_y\delta\psi_{k-1})$$

$$+ J_{xy}(\partial_x\delta\psi_{k-1}, \partial_y\delta\psi_1) + J_{xy}(\partial_x\delta\psi_2, \partial_y\delta\psi_{k-2}) + J_{xy}(\partial_x\delta\psi_{k-2}, \partial_y\delta\psi_2) + \ldots],$$

$$\ldots \tag{5a}$$

$$\delta\psi_k = 0 \text{ on } \partial D \text{ for } k = 1, 2, 3, \ldots \tag{5b}$$

Here, (5) gives a formal series of linearized equations and boundary conditions for computing $\delta\psi_k$ consecutively from $\delta\psi_1$ to increasingly higher-order term in the expansion of ψ in (5). The equations in (5a), however, are inconvenient to use, because the equation at each given order becomes increasingly complex as the order k increases. It is thus desirable to modify (5a) into a recursive form, and this can be done non-uniquely by first combining the equations in (5a) with $\nabla^2(f\psi_0) = \nabla^2\phi$ into a series of equations for ψ_k (instead of $\delta\psi_k$) and then adding properly selected higher-order terms to the equation for ψ_k at each order without affecting the order of accuracy of the equation. In particular, two different modifications will be made in the next two subsections. From these two modifications, the two types of iterative methods reviewed in the introduction for solving the NBE can be derived formally and systematically via the asymptotic expansion of ψ in (4).

2.2 Derivation of method-1

The equations in (5a) can be combined with $\nabla^2(f\psi_0) = \nabla^2\phi$ at $O(\varepsilon^0)$ into a series of equations for ψ_k defined in (4) as shown blow:

$$
\begin{aligned}
\nabla^2(f\psi_1) &= \nabla^2\phi + \varepsilon\nabla\cdot(\psi_0\nabla F) - 2\varepsilon J_{xy}(\partial_x\psi_0, \partial_y\psi_0),\\
\nabla^2(f\psi_2) &= \nabla^2\phi + \varepsilon\nabla\cdot(\psi_1\nabla F) - 2\varepsilon[J_{xy}(\partial_x\psi_0, \partial_y\psi_0) + \varepsilon J_{xy}(\partial_x\psi_0, \partial_y\delta\psi_1) + \varepsilon J_{xy}(\partial_x\delta\psi_1, \partial_y\psi_0)]\\
&= \nabla^2\phi + \varepsilon\nabla\cdot(\psi_1\nabla F) - 2\varepsilon[J_{xy}(\partial_x\psi_1, \partial_y\psi_1) - \varepsilon^2 J_{xy}(\partial_x\delta\psi_1, \partial_y\delta\psi_1)]\\
&= \nabla^2\phi + \varepsilon\nabla\cdot(\psi_1\nabla F) - \varepsilon 2J_{xy}(\partial_x\psi_1, \partial_y\psi_1) + O(\varepsilon^3),\\
\nabla^2(f\psi_3) &= \nabla^2\phi + \varepsilon\nabla\cdot(\psi_2\nabla F) - 2\varepsilon[J_{xy}(\partial_x\psi_1, \partial_y\psi_1) + \varepsilon^2 J_{xy}(\partial_x\psi_0, \partial_y\delta\psi_2) + \varepsilon^2 J_{xy}(\partial_x\delta\psi_2, \partial_y\psi_0)]\\
&= \nabla^2\phi + \varepsilon\nabla\cdot(\psi_2\nabla F) - 2\varepsilon[J_{xy}(\partial_x\psi_1, \partial_y\psi_1) + \varepsilon^2 J_{xy}(\partial_x\psi_1, \partial_y\delta\psi_2) + \varepsilon^2 J_{xy}(\partial_x\delta\psi_2, \partial_y\psi_1)\\
&\qquad - \varepsilon^3 J_{xy}(\partial_x\delta\psi_1, \partial_y\delta\psi_2) - \varepsilon^3 J_{xy}(\partial_x\delta\psi_2, \partial_y\delta\psi_1)]\\
&= \nabla^2\phi + \varepsilon\nabla\cdot(\psi_2\nabla F) - 2\varepsilon[J_{xy}(\partial_x\psi_2, \partial_y\psi_2) - \varepsilon^3 J_{xy}(\partial_x\delta\psi_1, \partial_y\delta\psi_2) - \varepsilon^3 J_{xy}(\partial_x\delta\psi_2, \partial_y\delta\psi_1)\\
&\qquad - \varepsilon^4 J_{xy}(\partial_x\delta\psi_2, \partial_y\delta\psi_2)]\\
&= \nabla^2\phi + \varepsilon\nabla\cdot(\psi_2\nabla F) - 2\varepsilon J_{xy}(\partial_x\psi_2, \partial_y\psi_2) + O(\varepsilon^4),\\
&\dots\\
\nabla^2(f\psi_k) &= \nabla^2\phi + \varepsilon\nabla\cdot(\psi_{k-1}\nabla F) - 2\varepsilon J_{xy}(\partial_x\psi_{k-1}, \partial_y\psi_{k-1}) + O(\varepsilon^{k+1}),\\
&\dots
\end{aligned}
\tag{6}
$$

Formally ψ_k is accurate up to $O(\varepsilon^k)$ and so is $\nabla^2(f\psi_k)$ on the left-hand side of the above k^{th} equation. This implies that the k^{th} equation is accurate only up to $O(\varepsilon^k)$, so the last term $O(\varepsilon^{k+1})$

(that represents all the high-order terms) on the right-hand side can be neglected without degrading the order of accuracy of the equation. This leads to the following recursive form of equation and boundary condition for solving the NBE iteratively:

$$\nabla^2(f\psi_k) = \nabla^2\phi + \varepsilon\nabla\cdot(\psi_{k-1}\nabla F) - 2\varepsilon J_{xy}(\partial_x\psi_{k-1}, \partial_y\psi_{k-1}), \tag{7a}$$

$$\psi_k = \psi_g \quad \text{on } \partial D \quad \text{for } k = 1, 2, 3, \ldots. \tag{7b}$$

If ε is sufficiently small to ensure the convergence of the asymptotic expansion in (5), then $\psi_k \to \psi$ gives the solution of the NBE in the limit of $k \to \infty$.

Substituting $\varepsilon\nabla F = \nabla f/f_o$ and $\varepsilon = R_o \equiv U/f_oL$ into (7) gives the dimensional form of (7):

$$\nabla^2(f\psi_k) = \nabla^2\phi + \nabla\cdot(\psi_{k-1}\nabla f) - 2J_{xy}(\partial_x\psi_{k-1}, \partial_y\psi_{k-1}), \tag{8a}$$

$$\psi_k = \psi_g \quad \text{on } \partial D. \tag{8b}$$

For f = constant, (8a) recovers (5) of Bushby and Huckle (1956), but this recursive form of equation is derived here formally and systematically via the asymptotic expansion of the solution in (4). Substituting the dimensional form of $\psi_k = \psi_{k-1} + \varepsilon^k\delta\psi_k$, that is, $\psi_k = \psi_{k-1} + \delta\psi_k$ into (8) gives

$$\nabla^2(f\delta\psi_k) = \nabla^2\phi - N(\psi_{k-1}), \tag{9a}$$

$$\delta\psi_k = 0 \text{ on } \partial D \text{ for } k = 1, 2, 3, \ldots \tag{9b}$$

where $N(\ )$ is the nonlinear differential operator defined in (1a). Analytically, (9a) is identical to (8a) but expressed in an incremental form. Numerically, however, solving $\delta\psi_k$ from (9) and updating $\psi_{k\text{-}1}$ to $\psi_k = \psi_{k\text{-}1} + \delta\psi_k$ iteratively does not give exactly the same solution as that obtained by solving ψ_k from (8) iteratively. According to our additional numerical experiments (not shown), the solutions obtained from (8) are less accurate (by about an order of magnitude for the case of $R_o = 0.1$) than their counterpart solutions obtained from (9), so the non-incremental form of boundary value problem in (8) will not be considered in this paper.

2.3 Derivation of method-2

The equation for ψ_k in (7) can be multiplied by 2 and rewritten into

$$2f\nabla^2\psi_k = 2\nabla^2\phi - 2\varepsilon(\nabla F)\cdot\nabla\psi_{k\text{-}1} - 4\varepsilon J_{xy}(\partial_x\psi_{k\text{-}1}, \partial_y\psi_{k\text{-}1}) + O(\varepsilon^{k+1}), \tag{10}$$

where $\psi_k = \psi_{k\text{-}1} + \varepsilon^k\delta\psi_k = \psi_{k\text{-}1} + O(\varepsilon^k)$ and $\nabla^2(f\psi_k) = f\zeta_k + (\nabla f)\cdot\nabla\psi_k + \nabla\cdot(\psi_k\nabla f) = f\zeta_k + \varepsilon(\nabla F)\cdot\nabla\psi_k + \varepsilon\nabla\cdot(\psi_k\nabla F) = f\zeta_k + \varepsilon(\nabla F)\cdot(\nabla\psi_{k\text{-}1}) + \varepsilon\nabla\cdot(\psi_{k\text{-}1}\nabla F) + O(\varepsilon^{k+1})$ are used. One can verify that $-4\varepsilon J_{xy}(\partial_x\psi_k, \partial_y\psi_k) = \varepsilon(\zeta_k^2 - A_k^2 - B_k^2) = \varepsilon\zeta_k^2 - \varepsilon(A_{k\text{-}1}^2 + B_{k\text{-}1}^2) + O(\varepsilon^{k+1})$ where $\zeta_k = \nabla^2\psi_k$, $A_k \equiv (\partial_x^2 - \partial_y^2)\psi_k$, $B_k \equiv 2\partial_x\partial_y\psi_k$, and $A_k = (\partial_x^2 - \partial_y^2)(\psi_{k\text{-}1} + \varepsilon^k\delta\psi_k) = A_{k\text{-}1} + O(\varepsilon^k)$ and $B_k = 2\partial_x\partial_y(\psi_{k\text{-}1} + \varepsilon^k\delta\psi_k) = B_{k\text{-}1} + O(\varepsilon^k)$ are used. Substituting these into (10) gives

$$\varepsilon\zeta_k^2 + 2f\zeta_k + 2\varepsilon(\nabla F)\cdot\nabla\psi_{k\text{-}1} - 2\nabla^2\phi - \varepsilon A_{k\text{-}1}^2 - \varepsilon B_{k\text{-}1}^2 = O(\varepsilon^{k+1}).$$

This leads to the following recursive form of equation that is accurate up to $O(\varepsilon^k)$:

$$\varepsilon\zeta_k^2 + 2f\zeta_k + 2\varepsilon(\nabla F)\cdot\nabla\psi_{k\text{-}1} - 2\nabla^2\phi - \varepsilon A_{k\text{-}1}^2 - \varepsilon B_{k\text{-}1}^2 = 0. \tag{11a}$$

Substituting $\varepsilon\nabla F = \nabla f/f_o$ and $\varepsilon = R_o \equiv U/f_oL$ into (11a) gives its dimensional form which can be rewritten into

$$(f + \zeta_k)^2 = M_{k\text{-}1} \equiv f^2 + 2\nabla^2\phi + A_{k\text{-}1}{}^2 + B_{k\text{-}1}{}^2 - 2(\nabla f)\cdot\nabla\,\psi_{k\text{-}1}. \tag{11b}$$

The non-negative condition of $(f + \zeta_k)^2 \geq 0$ requires $M_{k\text{-}1} \geq 0$ on the right-hand side of (11b). Also, as a quadratic equation of $f + \zeta_k$ for given ϕ and $\psi_{k\text{-}1}$, (11b) has two roots, but only the positive root, given by $f + \zeta_k = M_{k\text{-}1}{}^{1/2}$, is physically acceptable (because $f + \zeta_k \geq 0$ is required for stably balanced flow). This leads to the following recursive form of equation and boundary condition for solving the NBE iteratively:

$$\nabla^2\psi_k = -f + M_{k\text{-}1}{}^{1/2}, \tag{12a}$$

$$\psi_k = \psi_{\mathrm{g}} \quad \text{on } \partial D \quad \text{for } k = 1, 2, 3, \ldots. \tag{12b}$$

where $M_{k\text{-}1} \geq 0$ is ensured by setting $M_{k\text{-}1} = 0$ when the computed $M_{k\text{-}1}$ from the previous step becomes negative. Here, (12a) gives essentially the same recursive form of equation as that in (8) of Shuman (1957) for solving the NBE iteratively, but this recursive form of equation is derived here via the asymptotic expansion of the solution in (4).

3. Iterative procedures with optimal truncation and experiment design

3.1 Criterion for optimal truncation

When the Rossby number is not sufficiently small to ensure the convergence of the asymptotic expansion, the optimal truncation of the asymptotic expansion of ψ in (4) can be determined (Boyd, 1999) by an empirical criterion in the following dimensional form:

$$E[N(\psi_K)] = \min E[N(\psi_k)] \text{ for } k = K, K \pm 1, \dots K \pm m, \tag{13}$$

where $N(\ )$ is the function form defined in (1a), K is the number of optimal truncation, $E[N(\psi_k)] \equiv ||\varepsilon[N(\psi_k)]||'$, $||\ ||'$ denotes the root-mean-square (RMS) of discretized field of the variable inside $||\ ||'$ computed over all the interior grid points (excluding the boundary points) of domain D, and $\varepsilon[N(\psi_k)] \equiv [N(\psi_k) - N(\psi_t)]/||N(\psi_t)||' = [N(\psi_k) - \nabla^2\phi]/||\nabla^2\phi||'$ is the relative error of $N(\psi_k)$ with respect to $N(\psi_t)$ which is also the normalized (by $||\nabla^2\phi||'$) residual error of the NBE caused by the approximation of $\psi \approx \psi_k$, and ψ_t denotes the true solution. Here, $E[N(\psi_K)]$ is expected to be the global minimum of $E[N(\psi_k)]$. If $E[N(\psi_k)]$ does not oscillate as k increases, then it is sufficient to set $m = 1$ in (13). Otherwise, m should be sufficiently large to ensure $E[N(\psi_K)]$ be the global minimum of $E[N(\psi_k)]$.

3.2 Iterative procedures

The iterative procedure for method-1 performs the following steps:

1. Start from $k = 0$ and set $\psi_0 = \psi_g \equiv \phi/f$ in D and ∂D.
2. Substitute ψ_{k-1} ($= \psi_0$ for $k = 1$) into $N(\psi_{k-1})$ to compute the right-hand-side of (9a), and then solve the boundary value problem in (9) for $\delta\psi_k$.
3. Substitute $\psi_k = \psi_{k-1} + \alpha\delta\psi_k$ into $||N(\psi_k) - \nabla^2\phi||'$ and save the computed $||N(\psi_k) - \nabla^2\phi||'$ where α is an adjustable parameter in the range of $0 < \alpha \leq 1$.
4. If $k \geq 2m$, then find $\min||N(\psi_{k'}) - \nabla^2\phi||'$, say at $k' = K'$, for $k' = k, k - 1, \dots k - 2m$. If $K' < k - m$, then $K = K'$ and ψ_K gives the optimally truncated solution – the final solution that ends the iteration. Otherwise, go back to step 2.

When the Poisson solver (or SOR scheme) is used to solve boundary value problem in the above step 2, the iterative procedure designed for method-1 is named M1a (or M1b). For the Poisson solver used in this paper, the internally induced solution is obtained by using the scheme S2 described in section 2.1 of Cao and Xu (2011) and the externally induced solution obtained by using the Cauchy integral method described in section 4.1 of Cao and Xu (2011). For M1a with $Ro < 0.4$ (or $Ro = 0.4$), it is sufficient to set $m = 1$ and $\alpha = 1$ (or 1/2). For M1b, it is sufficient to set $m = 3$ and $\alpha = 1$.

The iterative procedure for method-2 performs the following steps:

1. Start from $k = 0$ and set $\psi_0 = \psi_g \equiv \phi/f$ in D and ∂D.
2. Substitute ψ_{k-1} into M_{k-1} defined in (11b) to compute the right-hand-side of (12a), and then solve the boundary value problem in (12) for ψ_k.
3. Compute and save $||N(\psi_k) - \nabla^2\phi||$'.
4. Perform this step as described above for step 4 of method-1.

When the Poisson solver (or SOR scheme) is used to solve boundary value problem in the above step 2, the iterative procedure designed for method-2 is named M2a (or M2b). For M2a and M2b, it is sufficient to set $m = 1$ and $\alpha = 1$.

3.3 Experiment design

To examine and compare the accuracies and computational efficiencies of the four iterative procedures, the true streamfunction field is formulated for a wavering jet flow by

$$\psi_t = -0.5UL\tanh[2y/L + 0.5\cos(\pi x'/L)] \quad (14)$$

and the associated velocity components are given by

$$u_t \equiv -\partial_y \psi_t = U\text{sech}^2[2y/L + 0.5\cos(\pi x'/L)] \tag{15a}$$

and $$v_t \equiv \partial_x \psi_t = 0.25\pi U\sin(\pi x'/L)\text{sech}^2[2y/L + 0.5\cos(\pi x'/L)], \tag{15b}$$

where $U = 20$ ms^{-1} is the maximum zonal speed of the wavering jet flow, $y = -0.25L\cos(\pi x'/L)$ is the longitudinal location (in y-coordinate) of the wavering jet axis as a function of $x' = x - x_0$, and x_0 is the zonal location of wave ridge. By setting the half-wavelength L to 2000, 1000 and 500 km, the flow fields formulated in (14) and (15) resemble wavering westerly jet flows on the synoptic, sub-synoptic and meso-α scales, respectively (as often observed on northern-hemisphere mid-latitude 500 hPa weather maps).

Four sets of experiments are designed to test and compare the iterative procedures with ψ_t given in (14) over a square domain of $D \equiv [-L \le x \le L, -L \le y \le L]$. The first set consists of four experiments to test the four iterative procedures (that is, M1a, M1b, M2a and M2b) on the synoptic scale by setting $L = 2000$ km and $x_0 = 0$ for ψ_t in (14). The second set also consists of four experiments but to test the four iterative procedures on the sub-synoptic scale by setting $L = 1000$ km and $x_0 = 0$ for ψ_t in (14). The third (or fourth) set still consists of four experiments to test the four iterative procedures on the meso-α scale by setting $L = 500$ km and $x_0 = 0$ (or L) for ψ_t in (14). Note that setting $x_0 = 0$ (or L) places the ridge (or trough) of the wavering jet in the middle of domain D, so the nonlinearly balanced flow used for the tests in the third (or fourth) set is curved anti-cyclonically (or cyclonically) in the middle of domain D. For simplicity, the Coriolis parameter f is assumed to be constant and set to $f = f_o = 10^{-4}$ s^{-1} in all the experiments. The Rossby number, defined by $Ro = U/f_o L$, is thus 0.1, 0.2 and 0.4 for L = 2000, 1000 and 500 km, respectively.

The true geopotential field, ϕ, is obtained by solving the Poisson equation, $\nabla^2\phi = N(\psi_t)$, numerically on a 51×51 grid over domain D with the boundary condition given by $\phi = f\psi_t$. In this case, ψ_t in (14) is also discretized on the same 51×51 grid over the same square domain, and is used to compute the right-hand side of $\nabla^2\phi = N(\psi_t)$ via standard finite-differencing. Then, ϕ is solved numerically by using the Poisson solver of Cao and Xu (2011). The SOR scheme can be also used to solve for ϕ, but the solution is generally less accurate than that obtained by using the Poisson solver. The NBE discretization error (scaled by $||\nabla^2\phi||'$) can be denoted and defined by

$$E(\nabla^2\phi) \equiv ||\nabla^2\phi - N(\psi_t)||'/||\nabla^2\phi||'. \tag{16}$$

This error is 3.25×10^{-3} (or 4.33×10^{-3}) for ϕ obtained by using the Poisson solver with L = 2000 (or 1000) but increases to 5.58×10^{-3} (or 5.78×10^{-3}) for ϕ obtained by using the SOR scheme. Thus, the solution obtained by using the Poisson solver is used as the input field of ϕ in the NBE to test the iterative procedures in each set of experiments.

4. Results of experiments

4.1 Results from first set of experiments

For this set of experiments, ψ_t and (u_t, v_t) are plotted in Fig. 1a, ψ_g and $(u_g, v_g) \equiv (-\partial_y\psi_g, \partial_x\psi_g)$ are plotted in Fig. 1b, the vorticity $\zeta_t \equiv \nabla^2\psi_t$ is plotted in Fig. 1c, and the geostrophic vorticity $\zeta_g \equiv \nabla^2 \psi_g$ is plotted in Fig. 1d. Figure 1c shows that the absolute voticity, defined by $f + \zeta_t$, is positive everywhere so the nonlinearly balanced wavering jet flow is inertially stable over the entire domain (see the proof in Appendix C of Xu, 1994). Figure 1c shows that the geostrophic vorticity ζ_g is larger than $-f/2$ ($= -f_o/2$) everywhere, so the NBE is elliptic over the entire domain and its associated boundary value problem in (1) is well posed.

The relative error of ψ_k with respect to ψ_t can be denoted and defined by

$$\varepsilon(\psi_k) \equiv (\psi_k - \psi_t)/\|\psi_t\|, \tag{17}$$

where || || denotes the RMS of discretized field of the variable inside || || computed over all the grid points (including the boundary points) of domain D. The accuracy of the solution ψ_k obtained during the iterative process in each experiment can be evaluated by the RMS of $\varepsilon(\psi_k)$, denoted and defined by

$$E(\psi_k) \equiv \|\varepsilon(\psi_k)\|, \tag{18}$$

where || || is defined in (17). The accuracy to which the NBE is satisfied by ψ_k can be measured by $E[N(\psi_k)]$ defined in (13).

Table 1 lists the values of $E(\psi_k)$ and $E[N(\psi_k)]$ for the initial guess ψ_0 ($= \psi_g$) in row 1 and the optimally truncated solutions ψ_K from the four experiments in rows 2-5. As shown in row 2 versus row 1 of Table 1, M1a reaches the optimal truncation at $k = K = 6$ where $E[N(\psi_k)]$ is reduced (from 0.120 at $k = 0$) to its minimum [$= 2.411\times10^{-3} < E(\nabla^2\phi) = 3.25\times10^{-3}$ – the NBE discretization error defined in (16)] with $E(\psi_k)$ reduced (from 2.43×10^{-2} at $k = 0$) to 4.87×10^{-4}.

Figure 2a shows that $E(\psi_k)$ reaches its minimum (= 4.79×10^{-4}) at k = 10. This minimum is slightly below $E(\psi_K) = 4.87\times10^{-4}$ but undetectable in real-case applications.

On the contrary, as shown in row 3 of Table 1 and Fig. 2b, M1b reaches the optimal truncation very slowly at $k = K = 38493$ where $E[N(\psi_k)]$ is reduced to its global minimum (= 1.81×10^{-2}) with $E(\psi_k)$ reduced to 1.68×10^{-3}. Here, $E[N(\psi_k)]$ has three extremely shallow and small local minima (at k = 32408, 38490 and 38497) not visible in Fig. 2b. These local minima are detected and passed by setting m = 3 in (13) for M1b. Clearly M1b is less accurate and much less efficient than M1a.

Figure 2c (or 2d) shows that M2a (or M2b) reaches the optimal truncation at $k = K = 19$ (or 26) where $E[N(\psi_k)]$ is reduced to its global minimum [= 3.55×10^{-2} (or 2.66×10^{-2})] with $E(\psi_k)$ reduced to 4.55×10^{-3} (or 2.69×10^{-3}), and $E(\psi_k)$ decreases continuously toward its minimum [= 2.45×10^{-3} (or $1.62\times\times10^{-3}$)] as k increases beyond K. Thus, M2a and M2b are less efficient and much less accurate than M1a for Ro = 0.1.

4.2 Results from second set of experiments

For this set of experiments, ψ_t and (u_t, v_t) have the same patterns as those in Fig. 1a, and ψ_g and (u_g, v_g) are similar to those in Fig. 1b, but the contour intervals of ψ_t and ψ_g are reduced by 50% as L is reduced from 2000 to 1000 km with Ro increased to 0.2, so the wavering jet flow is on the sub-synoptic scale. In this case, the nonlinearly balanced jet flow is still inertially stable over the entire domain since $\zeta_t > -f$ everywhere as shown in Fig. 3a, but $\zeta_g < -f/2$ in the two small yellow colored areas as shown in Fig. 3b, so the NBE becomes hyperbolic locally in this small area and the boundary value problem in (1) is not fully well posed.

In this case, as shown in row 2 versus row 1 of Table 2, M1a reaches the optimal truncation at $k = K = 13$ where $E[N(\psi_k)]$ is reduced (from 0.243 at $k = 0$) to its minimum [$= 5.23\times10^{-3}$ close to $E(\nabla^2\phi) = 4.33\times10^{-3}$] with $E(\psi_k)$ reduced (from 4.86×10^{-2} at $k = 0$) to 1.24×10^{-3}. The rapid descending processes of $E(\psi_k)$ and $E[N(\psi_k)]$ (not shown) are similar to those in Fig. 2a for M1a in the first set of experiments.

As shown in row 3 of Table 2, M1b takes $K = 48057$ iterations to reach the optimal truncation and the values of $E[N(\psi_k)]$ and $E(\psi_k)$ at $k = K$ are about four times larger than those from M1a. The extremely slow descending processes of $E(\psi_k)$ and $E[N(\psi_k)]$ (not shown) are similar to those in Fig. 2b for M1b in the first set of experiments. As shown in row 4 (or 5) of Table 2, M2a (or M2b) reaches the optimal truncation at $k = K = 26$ (or 35) and the values of $E[N(\psi_K)]$ and $E(\psi_K)$ are more than (or about) 4 times of those from M1a. Thus, M1a is still more accurate and much more efficient than M1b and is more efficient and much more accurate than M2a and M2b for $Ro = 0.2$, although the boundary value problem in (1) in this case is not fully (but nearly) well posed.

4.3 Results from third set of experiments

For this set of experiments, ψ_t and (u_t, v_t) have the same patterns as those in Fig. 1a but the contour interval of ψ_t is reduced 4 times as L is reduced from 2000 to 500 km with Ro increased to 0.4, so the wavering jet flow is on the meso-α scale. Figure 4a shows the fields of ψ_g and (u_g, v_g) for the nonlinearly balanced jet flow. This nonlinearly balanced jet flow is inertially unstable in the yellow colored area south of the ridge of wavering jet axis in the middle of domain D where $\zeta_t < -f$ as shown in Fig. 4c. Figure 4d shows that $\zeta_g < -f/2$ in the long and broad yellow colored area along and around the wavering jet, so the NBE is hyperbolic in this area and the boundary value problem in (1) becomes seriously ill-posed.

In this case, as shown in row 2 of Table 3 and Fig. 5a, M1a reaches the optimal truncation at $k = K = 2$ where $E[N(\psi_k)]$ is decreased (from 0.57 at $k = 0$) to its minimum (= 0.13), while $E(\psi_k)$ decreases from 9.72×10^{-2} at $k = 0$ to 8.20×10^{-2} at $k = K = 2$ and then to its minimum (= 7.38×10^{-2}) at $k = 6$. As k increases beyond 6, M1a diverges. Its optimally truncated solution ψ_K is merely slightly more accurate than the initial guess ψ_0. As shown in row 3 of Table 3 and Fig. 5b, M1b reaches the optimal truncation at $k = K = 10325$ where $E[N(\psi_k)]$ is decreased to its global minimum (= 0.15), while $E(\psi_k)$ decreases to 8.31×10^{-2} at $k = K$ and then to its minimum (= 7.68×10^{-2}) at $k = 23515$. Thus, M1b is still less accurate and much efficient than M1a.

Figure 5c (or 5d) shows that M2a (or M2b) reaches the optimal truncation at $k = K = 26$ (or 29) where $E[N(\psi_k)]$ is reduced to its minimum [= 0.11 (or 0.10)], while $E(\psi_k)$ is reduced to its minimum [= 8.24×10^{-2} (or 8.24×10^{-2})] at $k = 25$ (or 26) and then increases slightly to 8.25×10^{-2} (or 8.26×10^{-2}) at $k = K = 26$ (or 29). As shown in row 4 (or 5) versus row 2 of Table 3, $E(\psi_K)$ from M2a (or M2b) is larger than that from M1a, so M2a (or M2b) is still less accurate than M1a in this case.

Figure 6a (or 6b) shows that $\varepsilon(\psi_K)$ from M1a (or M1b) peaks positively and negatively in the middle of domain D as $\varepsilon(\psi_0)$ does in Fig. 4b but with slightly reduced amplitudes. Figure 6c (or 6d) shows that $\varepsilon(\psi_K)$ from M2a (or M2b) has a broad negative peak south of the ridge of wavering jet axis similar to that of $\varepsilon(\psi_0)$ in Fig. 4b but with a slightly enhanced amplitude.

In this case, M1a is still slightly more accurate than other three iterative procedures but it cannot effectively reduce the solution error in the central part of the domain where not only the NBE is hyperbolic (with $\zeta_g < -f/2$ as shown in Fig. 4d) but also the jet flow is strongly anti-cyclonically curved and subject to inertial instability (with $\zeta_t < -f$ as shown in Fig. 4c).

4.4 Results from fourth set of experiments

For this set of experiments, ψ_t and (u_t, v_t) are plotted in Fig. 7a. These fields represent the same nonlinearly balanced wavering westerly jet flow as that in the third set of experiments except that the wave fields are shifted by a half of wavelength so the jet flow is curved cyclonically in the middle of domain D. In this case, ψ_g and (u_g, v_g) are nearly the same as the half-wavelength shifted fields (not shown) from Fig. 4a but with small differences mainly along and around the trough and ridge lines due to the boundary condition, $\phi \equiv f\psi_g = f\psi_t$, used here along the two trough lines (instead of the two ridge lines in Fig. 4a) for solving ϕ from $\nabla^2\phi = N(\psi_t)$. Figure 7c shows the jet flow becomes inertially unstable in the two yellow colored areas (where $\zeta_t < -f$) around the west and east boundaries of domain D. Figure 7d shows that the NBE becomes hyperbolic in the long and broad yellow colored area (where $\zeta_g < -f/2$) that is nearly the same as the yellow colored area in Fig. 4d but half-wavelength shifted, so the area of $\zeta_g < -f$ (that is, the area of $\zeta_0 + f < 0$ in which the initial guess field is inertially unstable) in Fig. 4d is moved with the ridge line to the west and east boundaries in Fig. 7d. As the area of $\zeta_g < -f$ and area of $\zeta_t < -f$ are moved away from the domain center to the domain boundaries where ψ_t is known and given by ϕ/f, solving the NBE becomes less difficult in this fourth set of experiments than in the third set.

In this case, as shown in row 2 of Table 4 and Fig. 8a, M1a reaches the optimal truncation at $k = K = 7$ where $E[N(\psi_k)]$ is decreased (from 0.76 at $k = 0$) to its minimum (= 3.81×10^{-2}), while $E(\psi_k)$ decreases from 9.71×10^{-2} at $k = 0$ to 2.29×10^{-2} at $k = K = 7$ and then to its flat minimum (= 2.25×10^{-2}) at $k = 12$, so ψ_K is significantly more accurate than ψ_0 and slightly less accurate than ψ_k at $k = 12$ (which is undetectable in real-case applications). As shown in row 3 of Table 4 and Fig. 8b, M1b reaches the optimal truncation at $k = K = 31830$ where $E[N(\psi_k)]$ is decreased to its global minimum (= 4.54×10^{-2}), while $E(\psi_k)$ decreases to 2.37×10^{-2} at $k = K$ and then to its minimum (= 2.21×10^{-2}) at $k = 57586$. Thus, M1b is still much less efficient and less accurate than M1a.

Figure 8c (or 8d) shows that M2a (or M2b) reaches the optimal truncation at $k = K = 27$ (or 32) where $E[N(\psi_k)]$ is reduced to its minimum [= 5.42×10^{-2} (or 4.66×10^{-2})], $E(\psi_k)$ reduces to 3.03×10^{-2} (or 2.64×10^{-2}) at $k = K$ and then to its minimum [= 2.72×10^{-2} (or 2.43×10^{-2})] at $k =$ 36 (or 44), so M2a (or M2b) is still less efficient and less accurate than M1a in this case.

Figure 7b shows that $\varepsilon(\psi_0)$ has a broad positive (or negative) peak south (or north) of the trough of wavering jet axis in the middle of domain D. These broad peaks are mostly reduced by M1a as shown by $\varepsilon(\psi_K)$ in Fig. 9a but slightly less reduced by M1b as shown in Fig. 9b and less reduced by M2a (or M2b) as shown in Fig. 9c (or 9d). However, the small secondary negative peak of $\varepsilon(\psi_g)$ near the west (or east) boundary in Fig. 7b is reduced only about 30% by M1a (or M1b) as shown by $\varepsilon(\psi_K)$ in Fig. 9a (or 9b) and even less reduced by M2a (or M2b) as shown in Fig. 9c (or 9d). Thus, all the four iterative procedures have difficulties to reduce the errors of their optimally truncated solutions near the west and east boundaries where not only the NBE is hyperbolic (with $\zeta_g < -f/2$ as shown in Fig. 7d) but also the jet flow is subject to inertial instability (with $\zeta_t < -f$ as shown in Fig. 7c). Nevertheless, since the area of $\zeta_t < -f$ is moved with the ridge of wavering jet axis to the domain boundaries in Fig. 7c, all the four iterative procedures perform significantly better in this set of experiments than in the previous third set, as shown in Fig. 9 and Table 4 versus Fig. 6 and Table 3. In this case, M1a is still most accurate and M1b is still least efficient among the four iterative procedures.

5. Conclusions

In this paper, two types of previous iterative methods for solving the NBE are reviewed and revisited. The first type was originally proposed by Bolin (1955), in which the NBE is transformed into a linearized equation for a presumably small correction to the initial guess or the subsequently updated solution. The second type was originally proposed by Shuman (1955, 1957) and Miyakoda (1956), in which the NBE is rearranged into a quadratic form of the absolute vorticity and the positive root of this quadratic form is used in the form of Poisson equation to obtain the solution iteratively. These two types of methods are re-derived formally by expanding the solution asymptotically upon a small Rossby number (see section 2), and the re-derived methods are called method-1 and method-2, respectively.

Since the rearranged asymptotic expansion is not ensured to converge especially when the Rossby number is not sufficiently small, a criterion for optimal truncation of asymptotic expansion is proposed [see (13)] to obtain the super-asymptotic approximation of the solution based on the heuristic theory of asymptotic analysis (Boyd, 1999). In addition, the Poisson solver based on the integral formulas (Xu et al., 2011; Cao and Xu, 2011) is used versus the SOR scheme to solve the boundary value problem in each iterative step.

The four iterative procedures are tested with analytically formulated wavering jet flows on different spatial scales in four sets of experiments. The computational domain covers one full wavelength and is centered at the ridge of the wavering jet in the first three sets of experiments but centered at the trough in the last set. In the first set of experiments, the wavering jet flow is formulated on the synoptic scale [with the half wavelength L = 2000 km and the associated Rossby number Ro = 0.1]. In this case, the NBE is of the elliptic type over the entire domain and therefore its boundary value problem is well posed. In the second set of experiments, the wavering jet flow is formulated on the sub-synoptic scale [with L = 1000 km and Ro = 0.2]. In this case, the NBE is of the elliptic type nearly over the entire domain so that its boundary value problem is nearly well posed. In the third (or fourth) set of experiments, the wavering jet flow is formulated on the meso-α scale with Ro = 0.4, the wavering jet flow is curved anti-cyclonically (or cyclonically) in the middle of the domain where the absolute vorticity is locally negative (or strongly positive), and the NBE becomes hyperbolic broadly along and around the wavering jet so that its boundary value problem is seriously ill-posed.

The test results can be summarized as follows: For wavering jet flows on the synoptic and sub-synoptic scales, all the four iterative procedures can reach their respective optimal truncations and the solution error (originally from the initial guess – the geostrophic streamfunction) can be reduced at the optimal truncation by an order of magnitude or nearly so even when the NBE is not entirely elliptic. Among the four iterative procedures, M1a is most accurate and efficient while M1b is least efficient. The results for wavering jet flows on the synoptic and sub-synoptic scales are insensitive to the location of wavering jet in the computational domain. In particular, according to our additional experiments (not shown in this paper), when the wavering jet is shifted zonally by a half of wavelength (with the trough moved to the domain center), the solution errors become slightly smaller and the optimal truncation numbers for M1a and M1b (or M2a and M2b) become slightly smaller (or larger) than those listed in Tables 1 and 2. For wavering jet flows on the meso-α scale in which the NBE's boundary value problem is seriously ill-posed, the four iterative procedures still can reach their respective optimal truncations with the solution error reduced effectively for cyclonically curved part of the wavering jet flow but not for the anti-cyclonically curved part. In this case, M1a is still most accurate and efficient while M1b is least efficient.

In comparison with M1b, the high accuracy and efficiency of M1a can be explained by the fact that the solution obtained by the Poisson solver based on the integral formulas is not only more accurate but also smoother than the solution obtained by the SOR scheme in each step of nonlinear iteration. Consequently, in each next step, the nonlinear differential term on the right-hand side of the incremental-form iteration equation [see (9a)] is computed more accurately in M1a than in M1b and so is the entire right-hand side. This is especially true and important when the entire right-hand side becomes very small (toward zero) in the late stage of iterations, as it also explains why M1b reaches the optimal truncation much slower than M1a (see Tables 1–4). In comparison with M2a and M2b, the high accuracy and efficiency of M1a can be explained by the fact that the solution in M1a is updated incrementally and the increment is small relative to the entire solution and so is the error of the increment computed in each step of nonlinear iteration. On the other hand, the solution in M2a or M2b is updated entirely and the entire solution is large relative to the increment and so is the error of the entire solution computed in each step of nonlinear iteration. Moreover, the recursive form of equation [see (12)] used by M2a and M2b contains a square root term on its right-hand side, so it cannot be converted into an incremental form. Furthermore, this square root term must set to zero when the term inside the square root becomes negative, although the term inside the square root corresponds to the squared absolute vorticity. This problem is caused by the non-negative absolute vorticity assumed in the derivation of the recursive form of equation for M2a and M2b.

Cyclonically curved meso-α scale jet flows in the middle and upper troposphere are often precursors of severe weather especially when the curved jet flow evolves into a cut-off cyclone atop a meso-α scale low pressure system in the lower troposphere. In this case, M1a can be potentially and particularly useful for severe weather analyses in the context of semi-balanced dynamics (Xu, 1994; Xu and Cao, 2012). In addition, since the mass fields can be estimated from Advanced Microwave Sounding Unit (AMSU) observations, using the NBE to retrieve the horizontal winds in and around tropical cyclones (TC) from the estimated mass fields have potentially important applications for TC warnings and improving TC initial conditions in numerical predictions (Velden and Smith, 1983; Bessho et al, 2006). Applications of M1a in the aforementioned directions deserve continued studies. In particular, the gradient wind can be easily computed for the axi-symmetric part of a cut-off cyclone (or TC) and used to improve the initial guess for the iterative procedure. This use of gradient wind can be somewhat similar to the use of gradient wind associated with the axisymmetric part of a hurricane to improve the basic-state potential vorticity (PV) construction for hurricane PV diagnoses (Wang and Zhang, 2003; Kieu and Zhang, 2010). Furthermore, either the gradient wind or the optimal truncated solution from M1a can be used as a new improved initial guess. In this case, the asymptotic expansion can be reformulated upon a new small parameter associated with the reduced error of the new initial guess and this new small parameter can be smaller or much smaller than the Rossby number used for the asymptotic expansion in this paper. The reformulated asymptotic expansion may be truncated to yield a more accurate 'hyperasymptotic' approximation of the solution according to the heuristic theory of asymptotic analysis (see section 5 of Boyd, 1999). This approach deserves further explorations.

Acknowledgments. The authors are thankful to Dr. Ming Xue for reviewing the original manuscript and to the anonymous reviewers for their constructive comments and suggestions. This work was supported by the ONR Grants N000141712375 and N000142012449 to the University of Oklahoma (OU) and the NSF of China Grants 91937301 and 41675060 and the National Key Scientific and Technological Infrastructure Project "EarthLab". The numerical experiments were performed at the OU supercomputer Schooner. Funding was also provided to CIMMS by NOAA/Office of Oceanic and Atmospheric Research under NOAA-OU Cooperative Agreement #NA11OAR4320072, U.S. Department of Commerce.

REFERENCES

Arnason, G., 1958: A convergent method for solving the balance equation. *J. Meteor.*, **15**, 220-225.

Asselin, R., 1967: The operational use of the balance equation. *Tellus*, **19**, 24-32.

Bessho, K., M. Demaria, and J. Knaff, 2006: Tropical cyclone wind retrievals from the advanced microwave sounding unit: application to surface wind analysis. *J. Appl. Meteor.*, **45**, 399-415.

Bijlsma, S., and R. Hoogendoorn, 1983: A convergence analysis of a numerical method for solving the balance equation. *Mon. Wea. Rev.*, **111**, 997-1001.

Bolin, B., 1955: Numerical forecasting with the barotropic model. *Tellus*, **7**, 27-49.

Bolin, B., 1956: An improved barotropic model and some aspects of using the balance equation for three-dimensional flow. *Tellus*, **8**, 61-75.

Boyd, J. P., 1999: The devil's invention: Asymptotic, superasymptotic and hyperasymptotic series. *Acta Applicandae Mathematicae*, **56**, 1–98.

Bring, A., and Charasch, E., 1958: An experiment in numerical prediction with two non-geostrophic barotropic models. *Tellus*, **10**, 88-94.

Bushby, F. H., and V. M. Huckle, 1956: The use of a stream function in a two-parameter model of the atmosphere. *Quart. J. Roy. Meteor. Soc.*, **82**, No. 354, 409-418.

Cao, J. and Q. Xu, 2011: Computing streamfunction and velocity potential in a limited domain. Part II: Numerical methods and test experiments. *Adv. Atmos. Sci.*, **28**, 1445-1458.

Charney, J., 1955: The use of the primitive equations of motion in numerical forecasting. *Tellus*,

7, 22-26.

Charney, J. G., and M. E. Stern, 1962: On the stability of internal baroclinic jets in a rotating atmosphere. *J. Atmos. Sci*., **19**, 159-172.

Courant, R., and D. Hilbert, 1962: *Methods of Mathematical Physics*. Vol. II. Interscience, 830 pp.

Kieu, C. Q., and D.-L. Zhang, 2010: A piecewise potential vorticity inversion algorithm and its application to hurricane inner-core anomalies. J. Atmos. Sci., 67, 1745-1758.

Kuo, H. L., 1959: Finite amplitude three-dimensional harmonic waves on the spherical earth. *J. Meteor*., **16**, 524-534.

Liao, T., and T. Chow, 1962: On the method for solving the balance equation in finite difference form. *Acta Meteor. Sinica*, 32, 224-231.

Miyakoda, K., 1956: On a method of solving the balance equation. *J. Meteor. Soc. Japan*, **34**, 364-367.

Schubert, W. H., R. K. Taft, and L. G. Silvers, 2009: Shallow water quasi-geostrophic theory on the sphere. *J. Adv. Model. Earth Syst.*, **1**, No. 2, 1-17.

Shuman, F. G., 1955: A method for solving the balance equation. *Technical Memorandum* No. 6, Joint Numerical Weather Prediction Unit, 12 pp.

Shuman, F. G., 1957: Numerical methods in weather prediction: I. The balance equation. *Mon. Wea. Rev.*, **85**, 329–332.

Southwell, R. V., 1946: *Relaxation Methods in Theoretical Physics.* Oxford, Clarendon Press, 248 pp.

Velden, C. S., and W. L. Smith, 1983: Monitoring tropical cyclone evolution with NOAA satellite microwave observations. *J. Appl. Meteor.*, **22**, 714–724.

Wang, X., and D-L. Zhang, 2003: Potential vorticity diagnosis of a simulated hurricane. Part I: Formulation and quasi-balanced flow. *J. Atmos. Sci*., **60**, 1593-1607.

Xu, Q., 1994: Semibalance model—connection between geostrophic-type and balanced-type intermediate models. *J. Atmos. Sci*., **51**, 953-970.

Xu, Q., and J. Cao, 2012: Semibalance model in terrain-following coordinates. *J. Atmos. Sci.*, **69**, 2201–2206.

Xu, Q., J. Cao, and S. Gao, 2011: Computing streamfunction and velocity potential in a limited domain. Part I: Theory and integral formulae. *Adv. Atmos. Sci*., **28**, 1433-1444.

Zhu, T., D-L. Zhang, and F. Weng, 2002: Impact of the advanced microwave sounding unit measurements on hurricane prediction. *Mon. Wea. Rev*., **130**, 2416-2432.

Table 1. Values of $E(\psi_k)$ and $E[N(\psi_k)]$ listed in row 1 for the initial guess ψ_0 (= ψ_g) with $k = 0$ and in rows 2-5 for ψ_K from the four iterative procedures in the first set of experiments (with $Ro = 0.1$). Here, $E(\psi_k)$ is defined in (18), $E[N(\psi_k)]$ is defined in (13), k is the iteration number, and ψ_K is the optimally truncated solution at $k = K$.

	$E(\psi_k)$	$E[N(\psi_k)]$	k
ψ_0	2.43×10^{-2}	0.120	$k = 0$
M1a	4.87×10^{-4}	2.41×10^{-3}	$k = K = 6$
M1b	1.68×10^{-3}	1.81×10^{-2}	$k = K = 38493$
M2a	4.55×10^{-3}	3.55×10^{-2}	$k = K = 19$
M2b	2.69×10^{-3}	2.66×10^{-2}	$k = K = 26$

Table 2. As in Table 1 but for the second set of experiments (with $Ro = 0.2$).

	$E(\psi_k)$	$E[N(\psi_k)]$	k
ψ_0	4.86×10^{-2}	0.243	$k = 0$
M1a	1.24×10^{-3}	5.23×10^{-3}	$k =K = 13$
M1b	5.14×10^{-3}	2.20×10^{-2}	$k = K = 48057$
M2a	6.31×10^{-3}	4.17×10^{-2}	$k = K = 26$
M2b	3.96×10^{-3}	2.94×10^{-2}	$k = K = 35$

Table 3. As in Table 1 but for the third set of experiments (with $Ro = 0.4$ and $x_0 = 0$).

	$E(\psi_k)$	$E[N(\psi_k)]$	k
ψ_0	9.72×10^{-2}	0.57	$k = 0$
M1a	8.20×10^{-2}	0.13	$k = K = 2$
M1b	8.31×10^{-2}	0.15	$k = K = 10325$
M2a	8.25×10^{-2}	0.11	$k = K = 26$
M2b	8.26×10^{-2}	0.10	$k = K = 29$

Table 4. As in Table 1 but for the fourth set of experiments (with $Ro = 0.4$ and $x_0 = L$).

	$E(\psi_k)$	$E[N(\psi_k)]$	k
ψ_0	9.71×10^{-2}	0.76	$k = 0$
M1a	2.29×10^{-2}	3.81×10^{-2}	$k = K = 7$
M1b	2.37×10^{-2}	4.54×10^{-2}	k=K= 31830
M2a	3.03×10^{-2}	5.42×10^{-2}	$k = K = 27$
M2b	2.64×10^{-2}	4.66×10^{-2}	$k = K = 32$

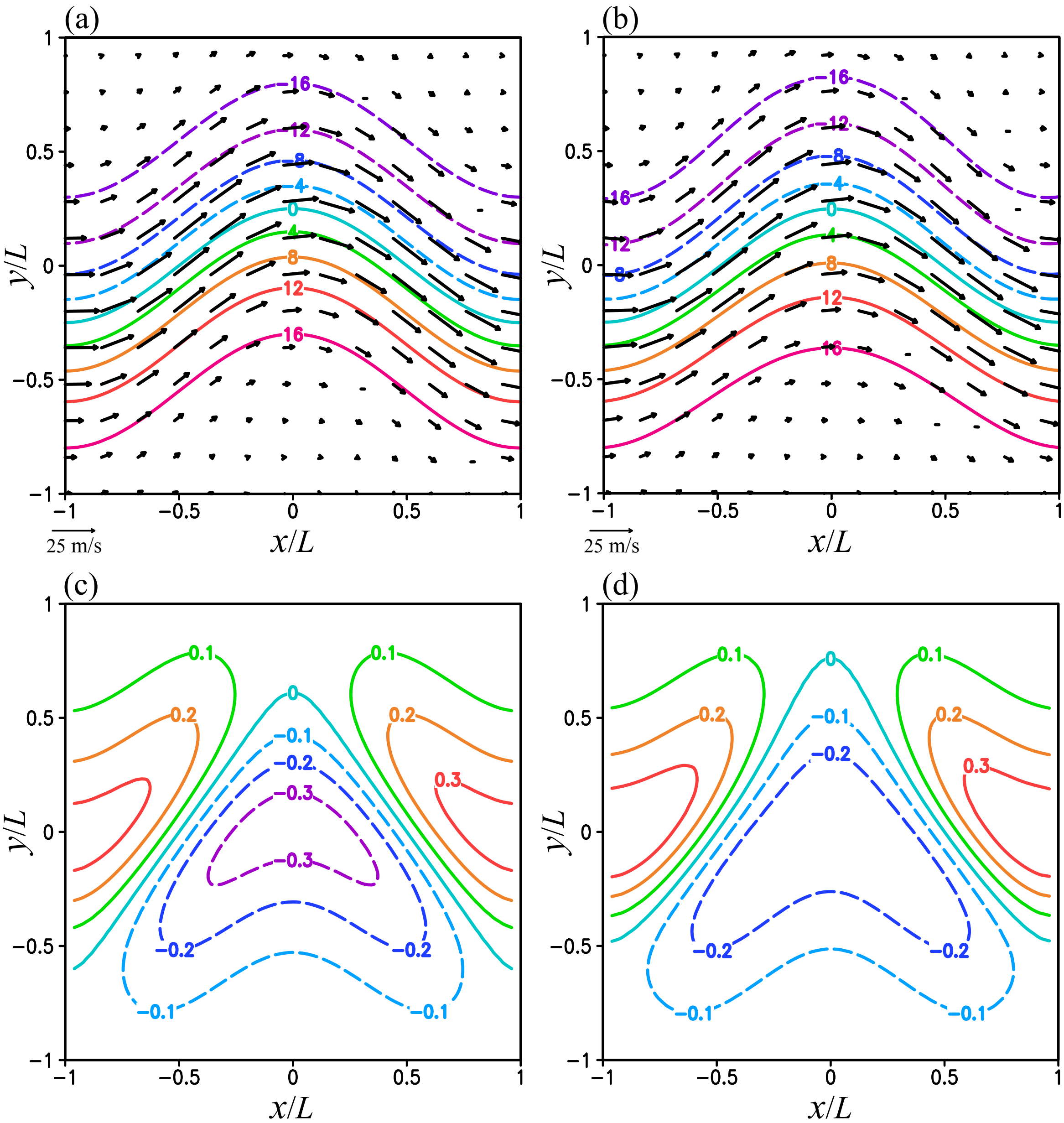

Fig. 1. (a) ψ_t plotted by color contours every 4.0 in the unit of 10^6 m^2s^{-1} and (u_t, v_t) plotted by black arrows over domain $D \equiv [-L \le x \le L, -L \le y \le L]$ with L = 2000 km for the first set of experiments. (b) As in (a) but for ψ_g and (u_g, v_g) with $\psi_g \equiv \phi/f$ and ϕ computed from ψ_t by setting $f = f_o = 10^{-4}$ s^{-1} as described in section 3.3. (c) Vorticity $\zeta_t \equiv \nabla^2\psi_t$ plotted by color contours every 0.1 in the unit of 10^{-4} s^{-1} over domain D. (d) As in (c) but for geostrophic vorticity $\zeta_g \equiv \nabla^2\psi_g$. The wavering jet axis is along the green contour of $\psi_t = 0$ in (a) with its ridge at $x = 0$ and two troughs at $x = \pm L$ on the west and east boundaries of domain D.

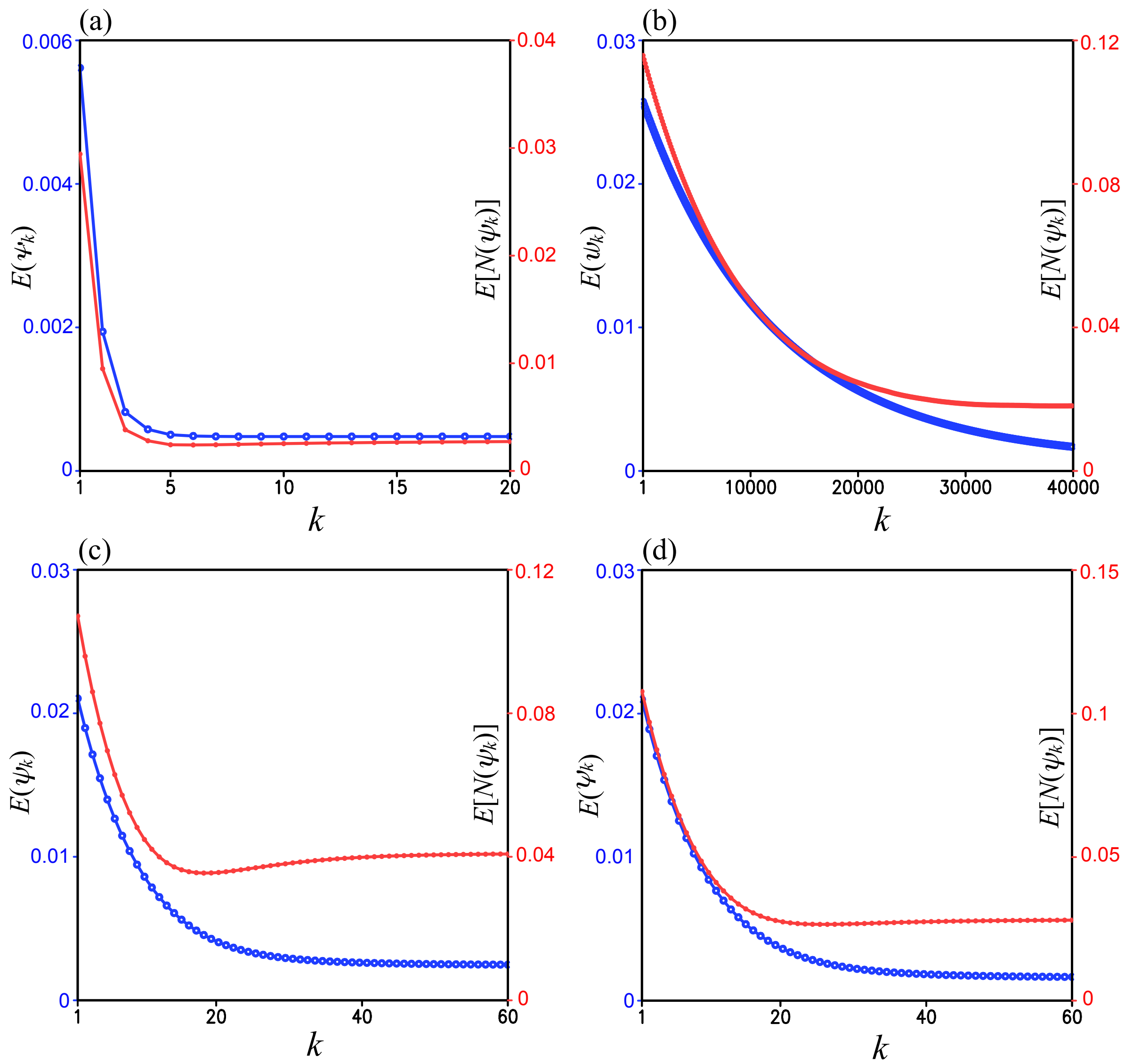

Fig. 2. (a) $E[N(\psi_k)]$ and $E(\psi_k)$ from M1a in the first set of experiments plotted by red and blue curves, respectively, as functions of k over the range of $1 \leq k \leq 20$. (b) As in (a) but from M1b plotted over the range of $1 \leq k \leq 4\times10^4$. (c) As in (a) but from M2a plotted over the range of $1 \leq k \leq 60$. (d) As in (c) but from M2b. In each panel, the ordinate of $E[N(\psi_k)]$ is on the left side labeled in red and the ordinate of $E(\psi_k)$ is on the right side labeled in blue.

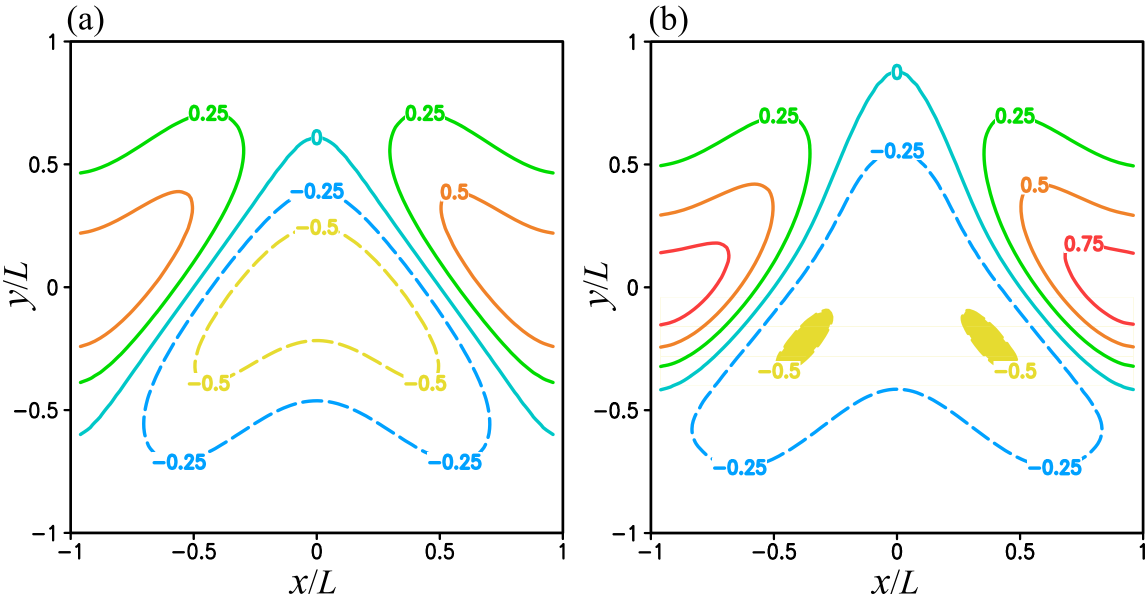

Fig. 3. (a) ζ_t plotted by color contours every 0.25 in the unit of 10^{-4} s^{-1} in domain D with L = 1000 km and Ro = 0.2 for the second set of experiments . (b) As in (a) but for ζ_g. As shown in (b), $\zeta_g < -f/2$ (= $-f_o/2$) in the two small yellow colored areas where the NBE becomes locally hyperbolic.

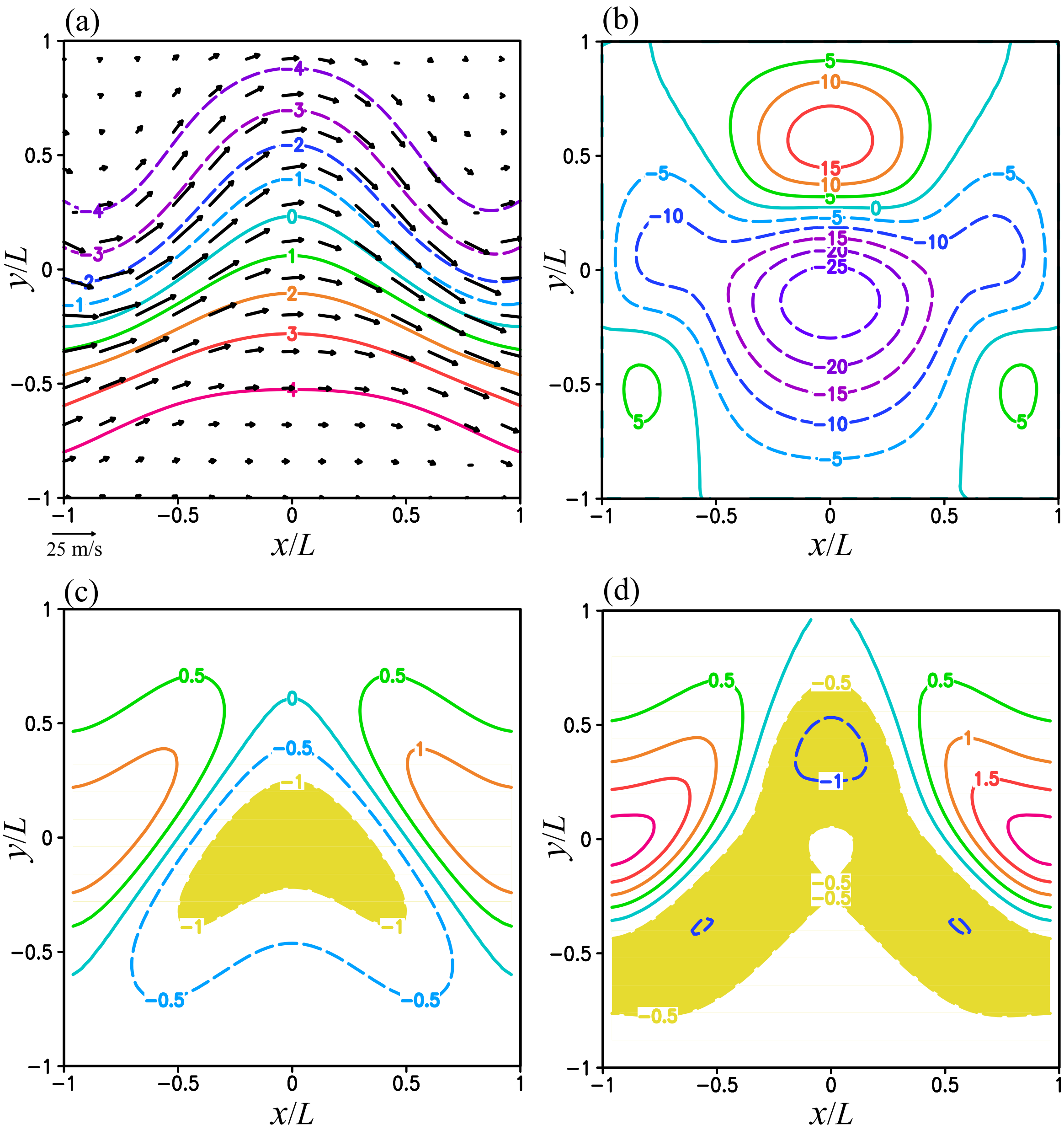

Fig. 4. (a) ψ_g plotted by color contours every 1.0 in the unit of 10^6 m^2s^{-1} and (u_g, v_g) plotted by black arrows over domain D with L = 500 km and Ro = 0.4 for the third set of experiments. (b) As in (a) but for $\varepsilon(\psi_0) = \varepsilon(\psi_g)$ plotted by color contours every 5.0 in the unit of 10^{-2}. (c) As in (a) but for ζ_t plotted by color contours every 0.5 in the unit of 10^{-4} s^{-1} in domain D. (d) As in (c) but for ζ_g. As shown in (c), $\zeta_t < -f$ in the yellow colored area south of the ridge of wavering jet axis where the jet flow becomes inertially unstable. As shown in (c), $\zeta_g < -f/2$ $(= -f_o/2)$ in the long and broad yellow colored area (along and around the wavering jet) where the NBE becomes hyperbolic.

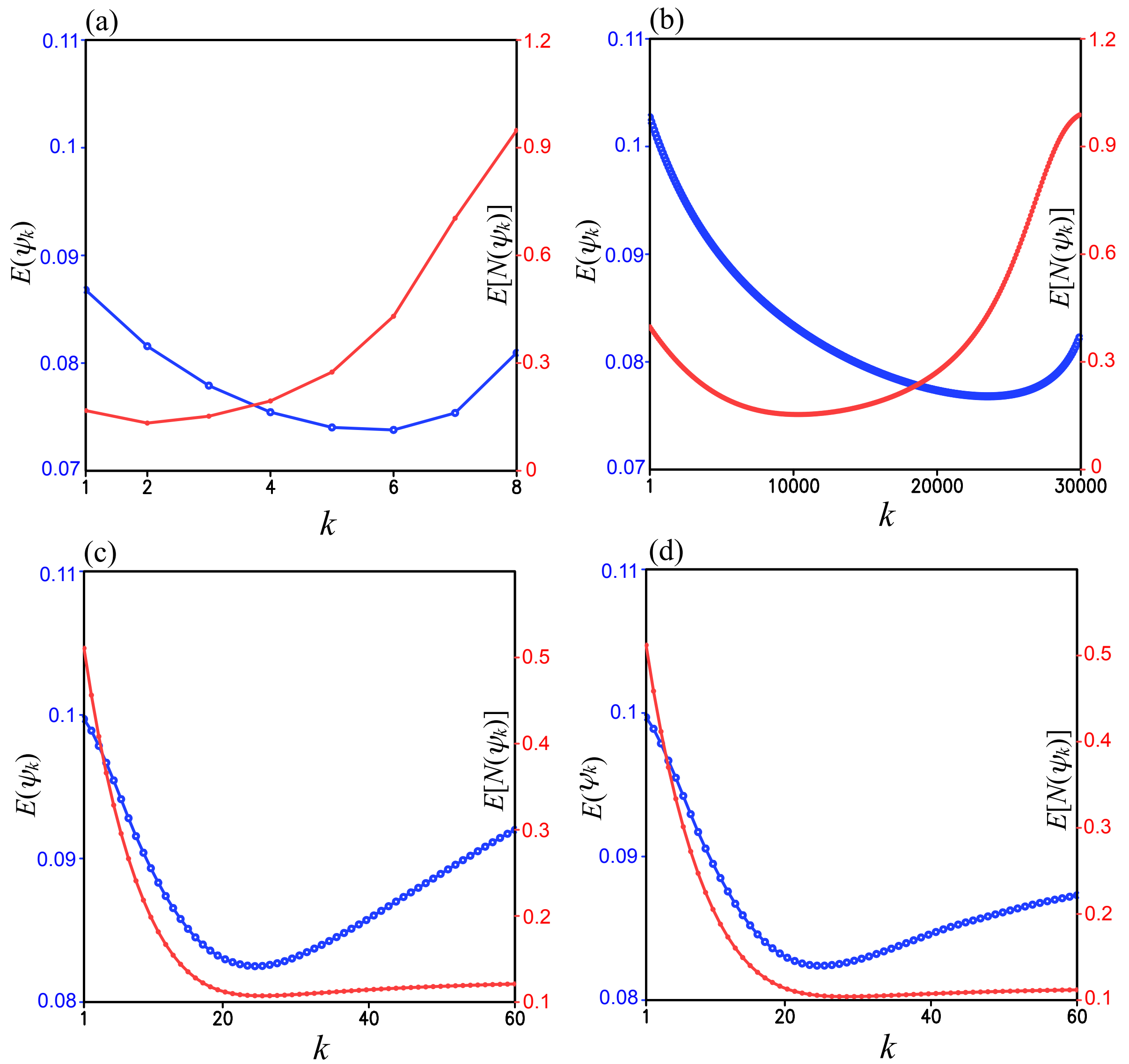

Fig. 5. (a) $E[N(\psi_k)]$ and $E(\psi_k)$ from M1a in the third set of experiments plotted by red and blue curves, respectively, as functions of k over the range of $1 \leq k \leq 8$, (b) As in (a) but from M1b plotted over the range of $1 \leq k \leq 3\times10^4$. (c) As in (a) but from M2a plotted over the range of $1 \leq k \leq 60$. (d) As in (a) but from M2b. In each panel, the ordinates of $E[N(\psi_k)]$ and $E(\psi_k)$ are placed and labeled as in Fig. 2.

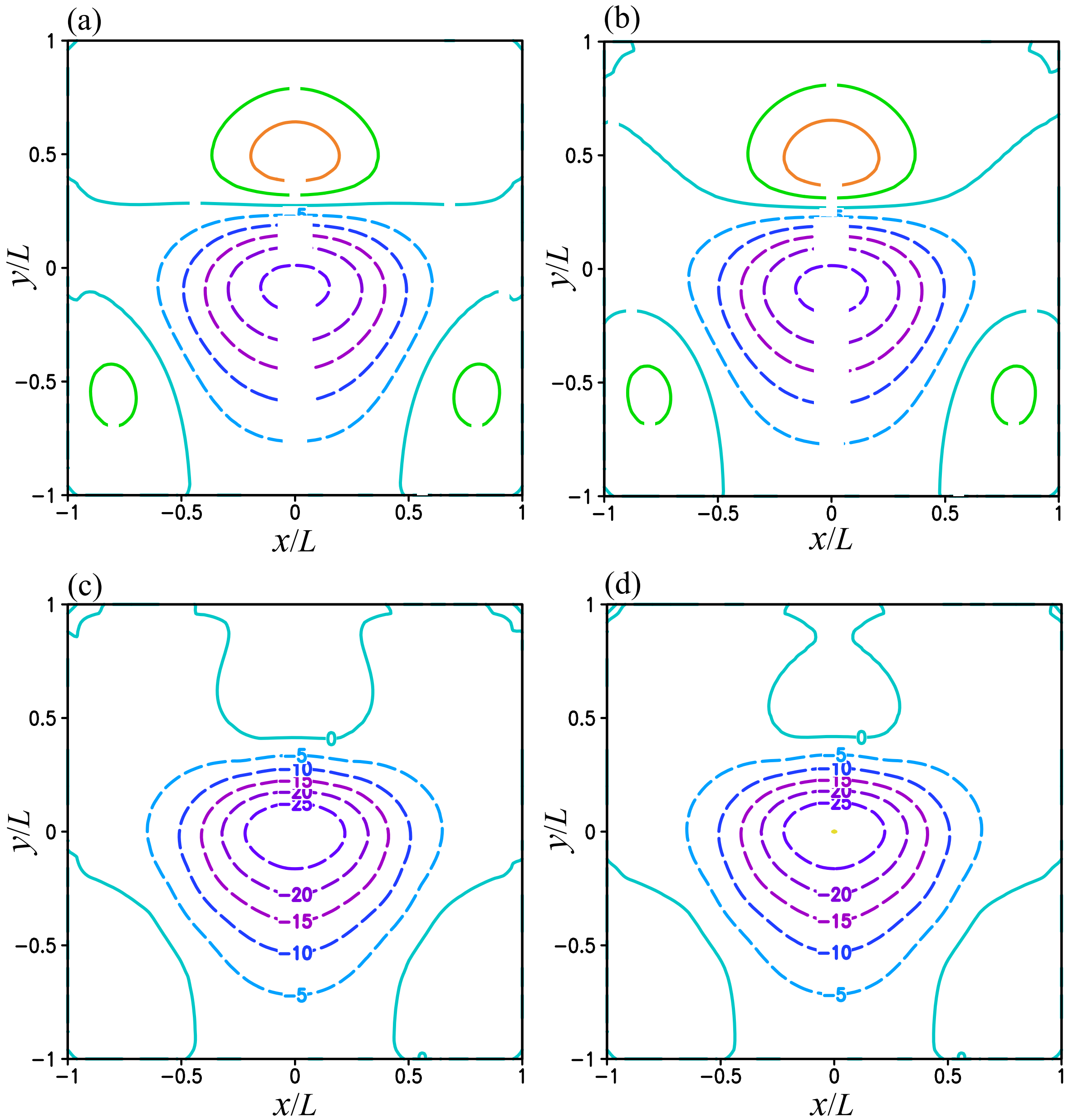

Fig. 6. $\varepsilon(\psi_K)$ plotted by color contours every 0.5 in the unit of 10^{-2} for ψ_K from (a) M1a, (b) M1b, (c) M2a and (d) M2b in the third set of experiments.

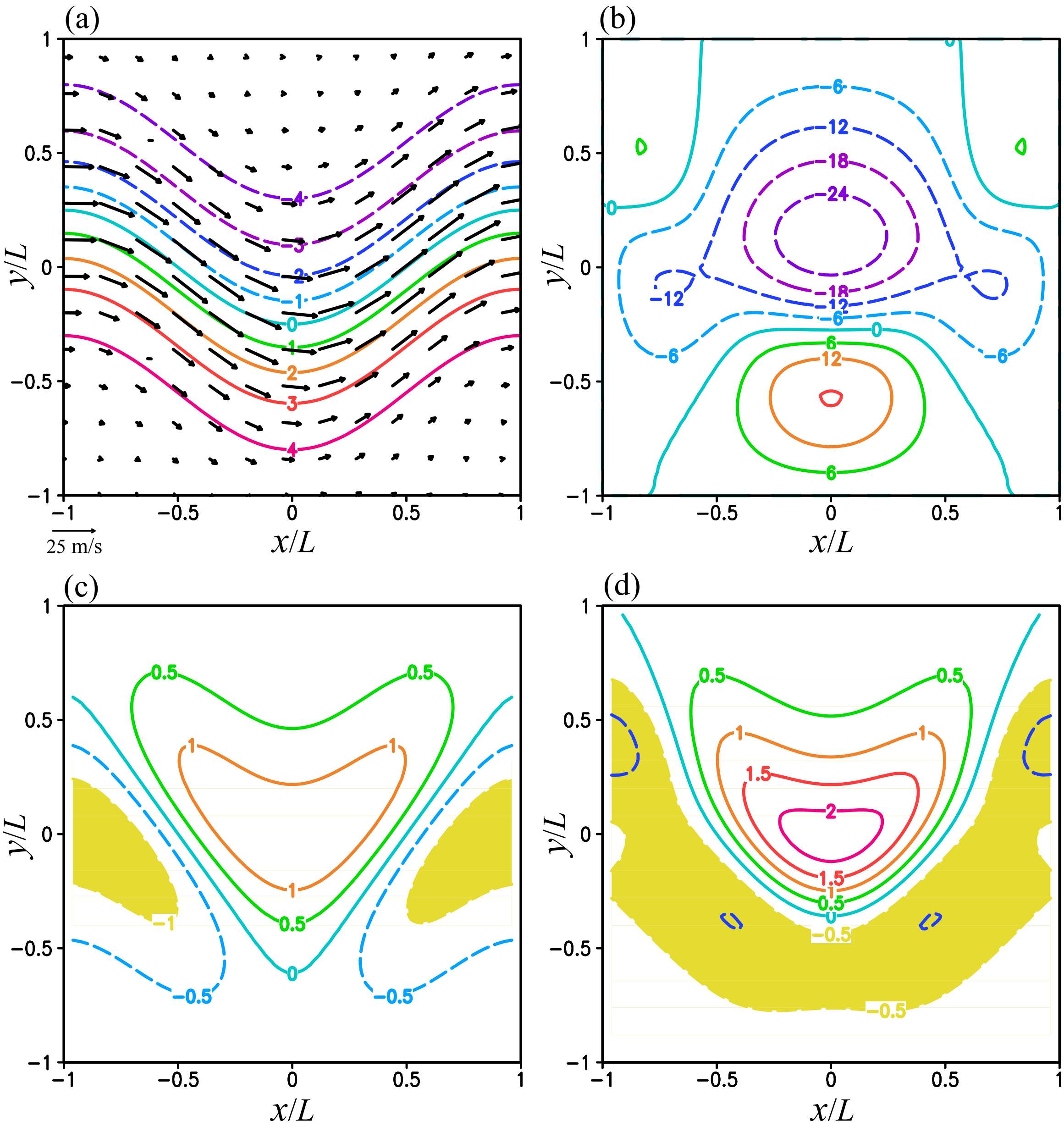

Fig. 7. (a) As in Fig. 4a but for ψ_t and (u_t, v_t) in the fourth set of experiments with L = 500 km and $x_0 = L$ (instead of $x_0 = 0$). (b) As in (a) but for $\varepsilon(\psi_0) = \varepsilon(\psi_g)$ plotted by color contours every 6.0 in the unit of 10^{-2}. (c) As in (a) but for ζ_t plotted by color contours every 0.5 in the unit of 10^{-4} s^{-1} in domain D. (d) As in (c) but for ζ_g.

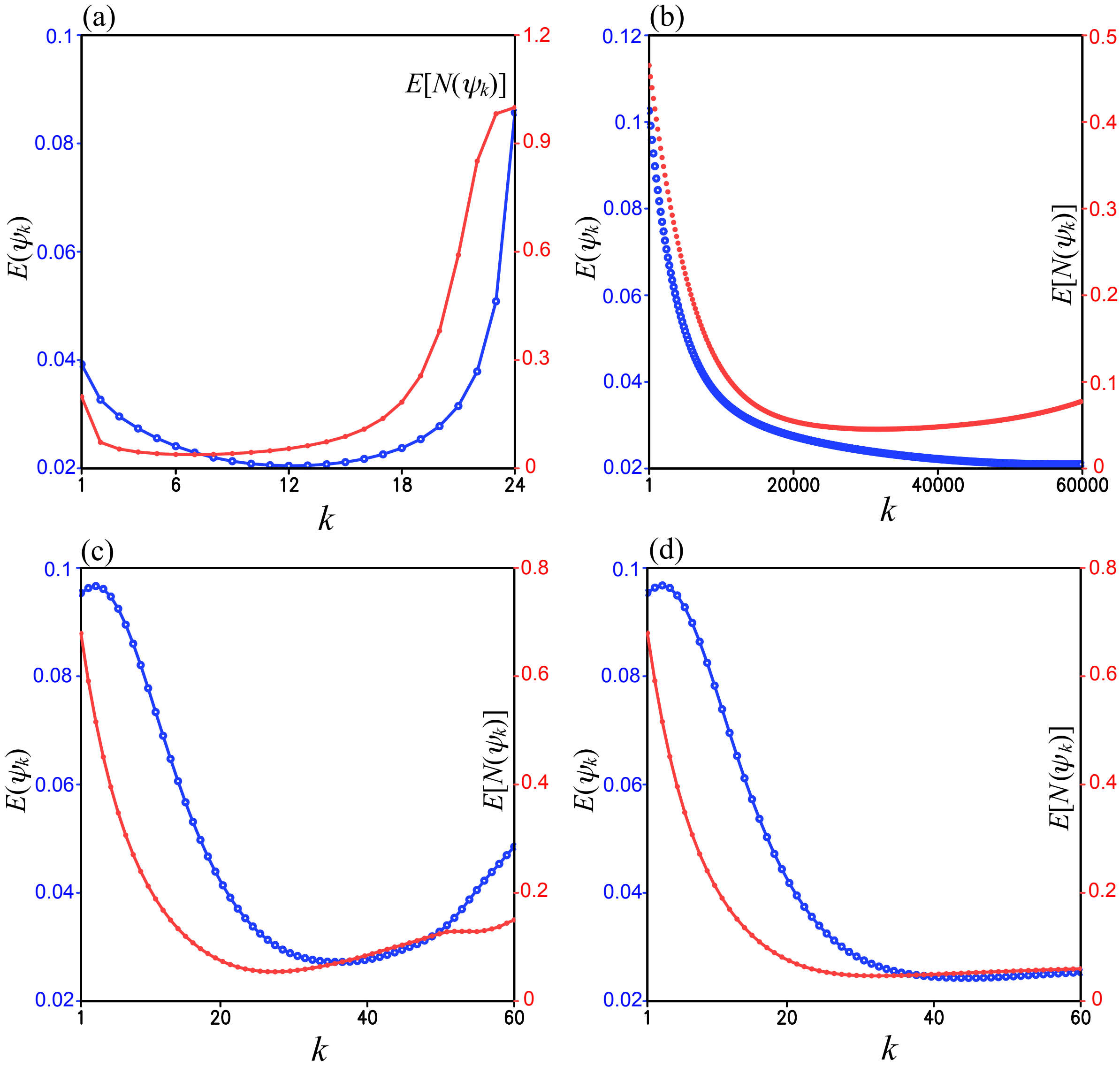

Fig. 8. (a) $E[N(\psi_k)]$ and $E(\psi_k)$ from M1a in the fourth set of experiments plotted by red and blue curves, respectively, as functions of k over the range of $1 \le k \le 24$, (b) As in (a) but from M1b plotted over the range of $1 \le k \le 6\times10^4$. (c) As in (a) but from M2a plotted over the range of $0 \le k \le 60$. (d) As in (a) but from M2b. In each panel, the ordinates of $E[N(\psi_k)]$ and $E(\psi_k)$ are placed and labeled as in Fig. 2.

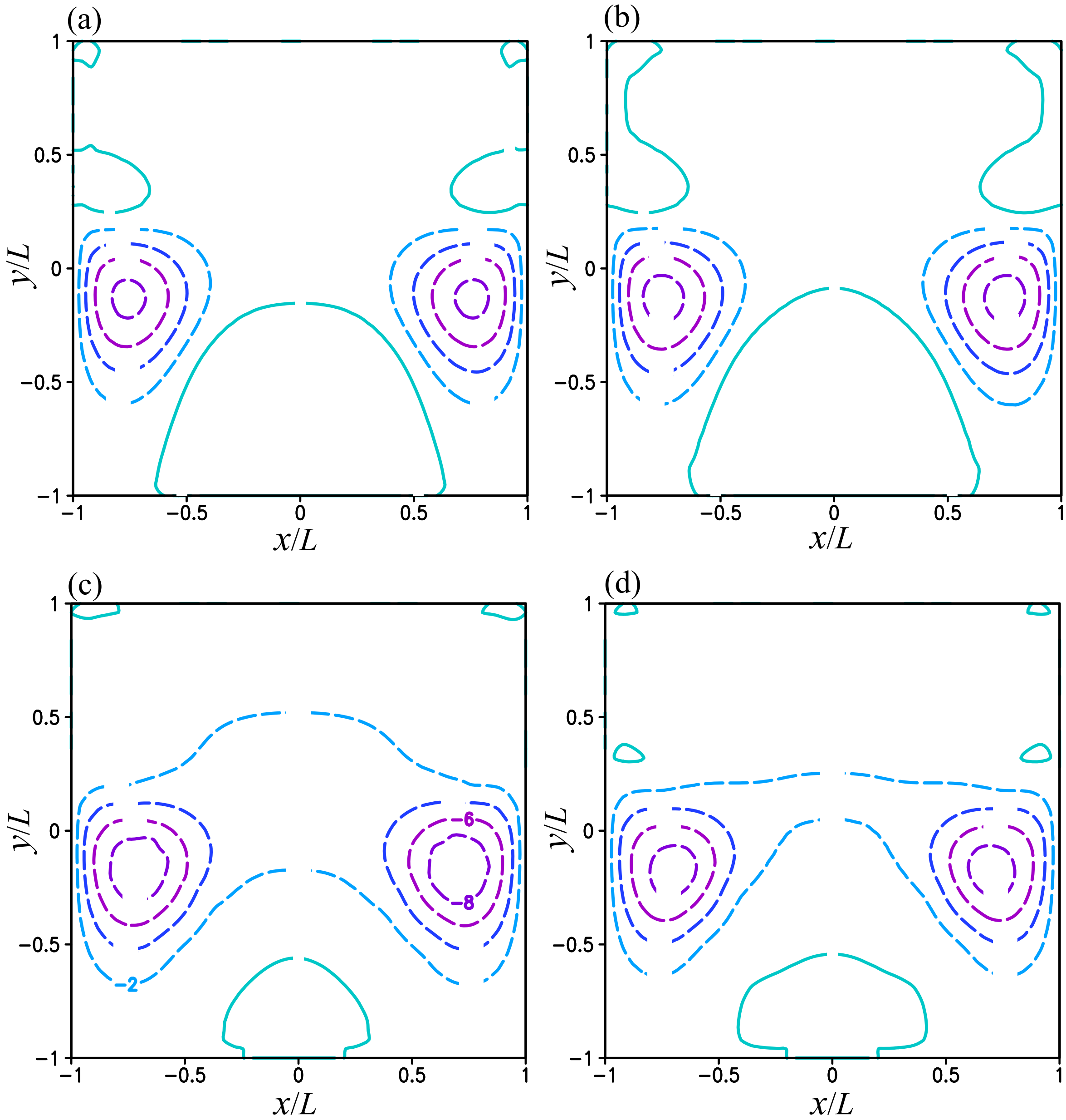

Fig. 9. $\varepsilon(\psi_K)$ plotted by color contours every 2.0 in the unit of 10^{-2} for ψ_K from (a) M1a, (b) M1b, (c) M2a and (d) M2b in the fourth set of experiments.